Analyzing the dihedral scattering component of P-band SAR signals for trunk permittivity estimation – a concept study

Anke Fluhrer, Hamed Alemohammad, Thomas Jagdhuber

Angaben zur Veröffentlichung / Publication details:

Fluhrer, Anke, Hamed Alemohammad, and Thomas Jagdhuber. 2025. "Analyzing the dihedral scattering component of P-band SAR signals for trunk permittivity estimation – a concept study." Science of Remote Sensing 11: 100236. https://doi.org/10.1016/j.srs.2025.100236.

Science of Remote Sensing 11 (2025) 100236

Contents lists available at ScienceDirect

Science of Remote Sensing

journal homepage: www.sciencedirect.com/journal/science-of-remote-sensing

Analyzing the dihedral scattering component of P-band SAR signals for trunk permittivity estimation – a concept study

Anke Fluhrer [a,*], Hamed Alemohammad [b], Thomas Jagdhuber [a,c]

[a] Microwaves and Radar Institute, German Aerospace Center (DLR), Muenchener Straße 20, Weßling, 82234, Germany
[b] Center for Geospatial Analytics & Graduate School of Geography, Clark University, Worcester, MA, 01610, USA
[c] Institute of Geography, University of Augsburg, Alter Postweg 118, 86159, Augsburg, Germany

ARTICLE INFO

Keywords:
Hybrid decomposition method
AirMOSS
Fresnel
X-Fresnel
Vegetation moisture
Microwave remote sensing

ABSTRACT

A new retrieval method, based on a hybrid decomposition technique and the extended (x-) Fresnel model, is proposed for estimating trunk permittivity from polarimetric P-band SAR observations. P-band SAR observations of NASA's Airborne Microwave Observatory of Subcanopy and Subsurface (AirMOSS) mission campaign are employed to test the proposed retrieval method at individual measuring stations across the U.S. between 2013 and 2015. In order to test the feasibility of the x-Fresnel model for such analyses and its sensitivity to required input parameters, a detailed sensitivity study revealed that at P-band frequencies there is a need to account for scattering losses, phase differences, as well as potential depolarization effects due to surface roughness. The decomposed dihedral scattering component increases with increasing vegetation cover from barren land at one station (control station) to homogeneously forested stations (target stations). Overall, no clear correlation between the amount of dihedral scattering and estimated trunk permittivity could be found, which is expected due to the architecture of the employed method. With the proposed approach, the estimated trunk permittivity varies between 2.4 and 59.7 [-], where the barren land and less dense forested stations show lower trunk permittivity. At these stations, the dihedral scattering is not the dominant scattering mechanism within the total SAR signal, which violates the physics of the proposed approach. At stations with dominant dihedral scattering, reasonable correlations (with r ranging from ± 0.1 to ± 0.64) between estimated trunk permittivity and AMSR2 relative water content (RWC), MODIS evapotranspiration (ET), in-situ measured relative humidity (RH), and air temperature (T_{air}) could be found. These parameters are used for analyzing the feasibility of the proposed approach as no in-situ trunk moisture measurements are available for the investigated stations and years. Hence, P-band SAR observations that exhibit sufficiently high dihedral scattering portions can be used for estimating trunk permittivity and extend the potential applications of remote sensing for climate research.

1. Introduction

Vegetation serves as a dynamic component within the soil-plant-atmosphere system (SPAS), influencing energy, carbon, and water fluxes at various scales (Arora, 2002; Orlowski et al., 2023). Vegetation moisture content is a key parameter in the regulation of energy exchange processes within ecosystems. It directly impacts transpiration rates, and hence, contributes to the redistribution of water vapor in the atmosphere, influencing regional precipitation patterns and the hydrological cycle. Through transpiration, vegetation modulates surface temperatures and influences local climate conditions. Further, changes in vegetation moisture content can alter canopy throughfall, runoff generation, soil moisture dynamics, and ground water recharge. These affect water availability and ecosystem resilience to drought and other extreme events (Notarnicola and Posa, 2007; Orlowski et al., 2023; Ruichen et al., 2023). Therefore, accurate estimation of vegetation moisture content, particularly at the trunk level, is essential for understanding forest ecosystems, modeling energy balance dynamics, and predicting climate responses (Konings et al., 2021). In the context of environmental monitoring, understanding vegetation moisture content is crucial for assessing ecosystem health and resilience (Gaulton et al., 2013). Moisture stress in vegetation can serve as an early indicator of environmental stressors, such as drought, heatwaves, or land use changes (Gaulton et al., 2013; Konings et al., 2021). Besides the

* Corresponding author.
E-mail address: Anke.Fluhrer@dlr.de (A. Fluhrer).

https://doi.org/10.1016/j.srs.2025.100236
Received 31 July 2024; Received in revised form 29 April 2025; Accepted 11 May 2025
Available online 12 May 2025

environmental importance, vegetation moisture influences interactions with electromagnetic waves, including those emitted and received by Synthetic Aperture Radar (SAR) systems. For one, the amount of vegetation moisture in canopy and trunk is directly related to the waves ability to penetrate the vegetation (Ulaby and Long, 2014; Fluhrer et al., 2022). Second, SAR observations are sensitive to vegetation, mainly due to the two-way canopy attenuation of reflected signals from the soil surface and the direct volume scattering from the canopy (Van Emmerik et al., 2015).

Besides biophysical variables, such as the vegetation water content and above ground biomass, several indices exist, such as the normalized difference vegetation index (NDVI), leaf area index (LAI), and normalized difference water index (NDWI). These have been used in remote sensing and ecological studies for characterizing vegetation properties as well as understanding ecosystem dynamics and environmental processes (Gao, 1996; Gu et al., 2008; Yihyun Kim et al., 2012). The variables and indices are mainly derived from optical, thermal, infrared, multi- and hyperspectral remote sensing, i.e., Landsat (Wulder et al., 2019), Terra/Aqua Moderate Resolution Imaging Spectroradiometer (MODIS) (e.g., Didan, 2021), and Sentinel-2 (Misra et al., 2020). In the field of active microwave remote sensing, only few attempts have been made in the past to retrieve vegetation moisture from SAR observations, e.g., (Jagdhuber, 2016; Quemada et al., 2021; Weiss, 2015). The recent review article of (Quemada et al., 2021) on vegetation water content monitoring based on remote sensing techniques proved the need for a remote sensing based method for estimating vegetation moisture from microwave SAR observations directly. That is why we are proposing an improved method for estimating trunk permittivity, the permittivity of the stem layer of woody plants between the ground surface and the tree canopy, from airborne polarimetric P-band SAR observations.

The motivation for this study originates from a previous study, where we have analyzed airborne P-band SAR signals across different landcover classes within the U.S. (Fluhrer et al., 2022). The aim of that study was the proof-of-concept of a revised hybrid decomposition method (combined eigen and model-based technique), specially designed for P-band (430 MHz) wavelengths. With this proposed hybrid decomposition method, we improved the removal of the vegetation component from the total SAR signal, a well-known problem within polarimetric decomposition techniques (He et al., 2016; Sato et al., 2012; van Zyl et al., 2011). By accounting for many different vegetation shapes and not just one as in many previous studies (Jagdhuber et al., 2015; Alemohammad et al., 2018), the vegetation component was modeled in a more realistic way. All these major adaptions led to a more robust and solid decomposition of the total P-band SAR signal into the individual scattering components from soil, vegetation and their combination (dihedral). The reader is referred to (Fluhrer et al., 2022) for more details.

One of the main findings of (Fluhrer et al., 2022) was that over dense forests, the normalized dihedral scattering component is the most dominant scattering mechanism within the total SAR signal. This finding was confirmed by other previous studies, which found predominantly dihedral scattering in strongly vertically oriented landcover classes like forests (Lucas et al., 2004; Moghaddam and Saatchi, 1995). Here, we want to conduct a follow-on study and analyze the decomposed dihedral scattering component from P-band SAR observations in perspective of estimating trunk permittivity. For that, we focus only on the landcover class 'forest' and try to evaluate which model is most suited for simulating P-band backscatters that are dominated by dihedral scattering scenarios. Further, we analyze whether trunk permittivity can be estimated from the decomposed dihedral scattering component, and how well the P-band SAR estimated trunk permittivity fits to in-situ field observations and remote sensing-based retrievals.

There have already been few attempts to estimate soil and trunk moisture from L-band (1.4 GHz) SAR signals over agricultures based on the dihedral scattering component (Weiss, 2015; Jagdhuber, 2016). However, these studies, for one, did apply less enhanced decomposition methods (i.e., referring to description of volume scattering component as well as static input parameters) for extracting the dihedral scattering component from the total SAR signal. Here, the enhanced decomposition method from (Fluhrer et al., 2022), which we use and adapt, improves the decomposition of the total SAR signal into the individual scattering components, and hence, improves the subsequent moisture retrieval. The adapted decomposition method allows, i.e., many different vegetation shapes depending on land cover conditions and variable input parameters. Second, in the previous published approaches, several assumptions have been made on important input parameters (e.g., concerning scattering losses, phase differences, or potential depolarization effects due to surface roughness) during model simulations (more details in sec. 3.). Some of them are justified because of the analysis of L-band wavelengths, some of them are made for the sake of simplicity. In this study, we show that several of these assumptions do not hold when analyzing P-band SAR signals. We adapt them accordingly based on detailed sensitivity studies and thorough model analyses (Sec. 4.).

2. Data

In this study, fully polarimetric P-band (430 MHz) SAR observations with a spatial resolution of ~90 m from the National Aeronautics and Space Administration's (NASA) Airborne Microwave Observatory of Subcanopy and Subsurface (AirMOSS) mission, conducted between 2013 and 2015 across North and Central America, are employed. We focus on the AirMOSS monitoring sites within the U.S. that are covered by forests, namely Howland Forest, ME, Harvard Forest, MA, Duke Forest, NC, and Metolius, OR. While three sites are located on the east coast, one site is located on the west coast of the U.S. (Fig. 1). Hence, Metolius is rather characterized by a temperate climate with dry summers (Csb), almost similar to Duke with a temperate climate but mild summers (Cfa), while Harvard and Howland are characterized by cold humid continental climate with warm summers and significant precipitation in all seasons (Dfb) (Peel et al., 2007). This means that Howland and Harvard are described by a boreal transitional or mixed forest, Duke is covered by a temperate or mixed forest as well as croplands, while Metolius is characterized by a temperate, evergreen needle-leaf forest (Alemohammad et al., 2018).

Due to missing input parameters at comparable spatial resolution to the AirMOSS observations, we focus only on single stations within each monitoring site, where in-situ measurements are available. For one, in-situ measured soil moisture is used as input to the retrieval method for estimating trunk permittivity. Second, in-situ measurements of relative humidity (RH; [%]) and air temperature (T_{air}; [°C]) are used for comparison later on.

The locations of in-situ measuring stations are shown in Fig. 1. It can be seen that the forest density varies at each site around the employed stations. We have no forest around the station Durham 11 W (control station) from the US Climate Reference Network (US-CRN) (Bell et al., 2013) within the SAR pixel footprint at monitoring site Duke, NC (Fig. 1B), partly sparsely forested stations within Metolius, OR, from the AmeriFlux (2022) and Cosmic-ray Soil Moisture Observing System (COSMOS) (Montzka et al., 2017) networks (Fig. 1A), and homogeneously dense forested stations within Harvard Forest, MA, and Howland Forest, ME, from the AmeriFlux and COSMOS networks or the Harvard University (Munger and Hadley, 2023) (Fig. 1C and D).

Due to the lack of in-situ measured trunk permittivity observations at the test sites between 2013 and 2015, we focus on the comparison of retrieval results with suitable (trunk permittivity related) parameters of the soil-plant-atmosphere system (SPAS). For that, we are using relative water content (RWC; [%]) of vegetation at 10 km spatial resolution from the Advanced Microwave Scanning Radiometer 2 (AMSR2) C-band radiometer sensor of the Japan Aerospace Exploration Agency (JAXA) (Jeu and Owe, 2014), and evapotranspiration (ET; [mm/day]) at 500 m spatial resolution from NASA's Moderate Resolution Imaging Spectroradiometer (MODIS) sensor on Terra (Running et al., 2017). This is no direct validation of the proposed method and emphasizes the need for

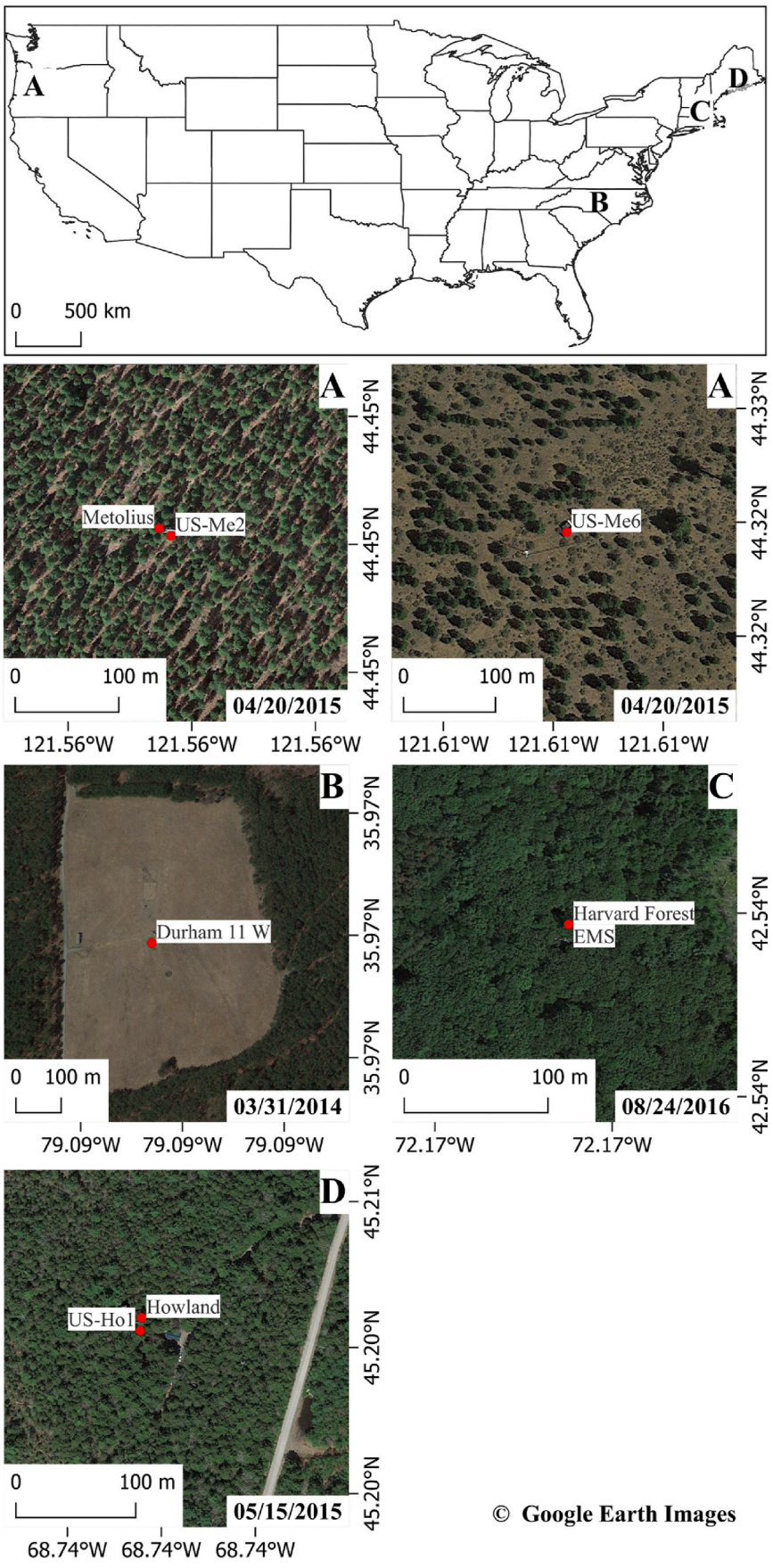

(caption on next page)

Fig. 1. Overview of the eight employed in-situ measuring stations within each ~90 m x ~90 m SAR footprint. A) Metolius, OR, with the stations US-Me2, US-Me6, and Metolius from the AmeriFlux and COSMOS network, respectively. B) Duke Forest, NC, with the station Durham 11 W from the US-CRN network. C) Harvard Forest, MA, with the stations Harvard Forest and EMS from the COSMOS network and the Harvard University, respectively. D) Howland Forest, ME, with the stations US-Ho1 and Howland from the AmeriFlux and COSMOS network respectively. Optical images are from Google Earth Pro© with the respective recording dates in the lower right corners. Political state boundaries of the U.S. in the upper plot are from (Homeland Infrastructure Foundation-Level Data (HIFLD), 2012).

in-situ trunk permittivity measurements in the future. The time series of in-situ measured T_{air} and RH as well as RWC are smoothed over time and cleaned for daily dynamics using the Savitzky-Golay filter (Savitzky and Golay, 1964) with a window size of 21 (days), while for the ET time series a window size of 3 (21 days) is used, due to the 8-daily temporal resolution.

3. Methods

For the retrieval of trunk permittivity (ε_t, [−]) from P-band SAR signals, the decomposed dihedral scattering component is compared to model simulations of the dihedral scattering mechanism. Through the best fit (minimum error approach) between the remote sensing information and the model simulations, the final permittivity is estimated. The comparison of data and model is performed on the level of the dihedral scattering angle α_d and the dihedral scattering intensity f_d. Both parameters can be retrieved by decomposing the P-band SAR signal as well as from forward scattering model simulations. In this study, we tested the common known Fresnel model and the extended (x-) Fresnel model for simulating the dihedral scattering components.

3.1. Fresnel scattering model

For simulations of the model-based dihedral scattering angle $\alpha_d^{Fresnel}$ and dihedral intensity $f_d^{Fresnel}$, the well-known Fresnel model, e.g., (Freeman and Durden, 1998; Ulaby and Long, 2014; Yamaguchi et al., 2006), is used.

First, the horizontal (1) and vertical (2) reflection coefficients for respective soil (s) and trunk (t) are calculated based on the incidence angle Θ_i as well as the permittivity ε (Cloude, 2010; Jagdhuber, 2016):

$$R_H^{s/t} = \frac{cos\Theta_{s/t} - \sqrt{\varepsilon_{s/t} - sin^2\Theta_{s/t}}}{cos\Theta_{s/t} + \sqrt{\varepsilon_{s/t} - sin^2\Theta_{s/t}}}, \tag{1}$$

$$R_V^{s/t} = \frac{\varepsilon_{s/t}\, cos\Theta_{s/t} - \sqrt{\varepsilon_{s/t} - sin^2\Theta_{s/t}}}{\varepsilon_{s/t}\, cos\Theta_{s/t} + \sqrt{\varepsilon_{s/t} - sin^2\Theta_{s/t}}}, \tag{2}$$

with $\Theta_s = \Theta_i$ and $\Theta_t = \pi/2 - \Theta_i$.

Second, the model-based $\alpha_d^{Fresnel}$ and $f_d^{Fresnel}$ can be estimated (Jagdhuber, 2016):

$$\alpha_d^{Fresnel} = \frac{R_{sH}R_{tH} - R_{sV}R_{tV}e^{i\varphi}}{R_{sH}R_{tH} + R_{sV}R_{tV}\, e^{i\varphi}}, \tag{3}$$

$$f_d^{Fresnel} = \frac{{m_D}^2}{2}\left|R_{sH}R_{tH} + R_{sV}R_{tV}e^{i\varphi}\right|^2, \tag{4}$$

with

$$m_D^{expo} = e^{-2k*s*cos\Theta_i}, \tag{5}$$

$$m_D^{Gauss} = e^{-2k^2*s^2*cos{\Theta_i}^2}. \tag{6}$$

The loss factor m_D [−], for exponential or Gaussian autocorrelation function (ACF) respectively, accounts for scattering losses (e.g., due to roughness) at the soil plane on the dihedral scattering intensity. Besides Θ_i, m_D depends on the wave number k [cm^{-1}] and the vertical root mean square (RMS) height s [cm] in order to reflect natural, lossy surfaces with variable roughness (Jagdhuber, 2016). k is dependent on the wavelength (~69.7 cm at 430 MHz) of the employed SAR data and set to $k = 2\pi/\lambda = 901.2\ cm^{-1}$ in this study. The phase angle φ [°] in the term $e^{i\varphi}$ of equations (3) and (4) expresses the phase differences between horizontal and vertical polarized backscatters (Jagdhuber, 2016). For the assumption of negligible propagation in oriented vegetation, as emphasized in previous L-band studies (Weiss, 2015; Jagdhuber, 2016), $\varphi = 0°$ and hence, $e^{i\varphi}$ becomes zero. Whether this assumption holds also for P-band backscatters will be analyzed in more detail in sec. 4.

3.2. Extended fresnel scattering model

Complementary to the Fresnel model (Sec. 3.1.), we are additionally using the x-Fresnel model from (Jagdhuber, 2016) in order to examine the most suitable scattering model for P-band analyses. The x-Fresnel model computes the Fresnel reflection coefficients of the soil and trunk scattering plane in the same way as the standard Fresnel model (Eqs. (1) and (2)), but additionally accounts for potential phase differences between horizontal and vertical polarized backscatters by calculating the model-based dihedral scattering angle $\alpha_d^{x-Fresnel}$ and intensity $f_d^{x-Fresnel}$ in a more sophisticated way (Jagdhuber, 2016):

$$\alpha_d^{x-Fresnel} = T_{12}^D / T_{22}^D, \tag{7}$$

$$f_d^{x-Fresnel} = {m_D}^{2*}\, T_{22}^D, \tag{8}$$

with

$$\begin{aligned} T_{12}^D = &-\frac{1}{4}\left(R_V^{s\,2} - R_H^{s\,2}\right)\left(R_V^{t\,2}e^{i\varphi} + R_H^{t\,2}\right)sinc(2\theta_1) \\ &- \left(R_V^{t\,2}e^{i2\varphi} - R_H^{t\,2}\right)\left(\frac{1}{16}\left(3R_V^{s\,2} + 2R_V^sR_H^s + 3R_H^{s\,2}\right.\right. \\ &\left.\left. + \left(R_V^s - R_H^s\right)^2 sinc(4\theta_1)\right)\right), \end{aligned} \tag{9}$$

and

$$\begin{aligned} T_{22}^D = &\frac{1}{16}\left(\left(2R_V^sR_H^s\left(R_V^{t\,2}e^{i2\varphi} + 6R_V^tR_H^te^{i\varphi} + R_H^{t\,2}\right)\right.\right. \\ &+ R_V^{s\,2}\left(3R_V^{t\,2}e^{i2\varphi} + 2R_V^te^{i\varphi}R_H^t + 3R_H^{t\,2}\right) \\ &\left.+ R_H^{s\,2}\left(3R_V^{t\,2}e^{i2\varphi} + 2R_V^te^{i\varphi}R_H^t + 3R_H^{t\,2}\right)\right) \\ &+ 4\left(\left(R_V^{s\,2} - R_H^{s\,2}\right)\left(R_V^{t\,2}e^{i2\varphi} - R_H^{t\,2}\right)sinc(2\theta_1)\right) \\ &\left.+ \left(\left(R_V^s - R_H^s\right)^2\left(R_V^te^{i\varphi} - R_H^t\right)^2 sinc(4\theta_1)\right)\right). \end{aligned} \tag{10}$$

Here, the rotation limit angle θ_1 [°] is used 'to account for soil-roughness induced depolarization' (Jagdhuber, 2016). In previous L-band studies over agricultural areas, θ_1 was always assumed to be zero, neglecting any potential depolarization due to surface roughness (Weiss, 2015; Jagdhuber, 2016). How this rotation limit angle affects the simulation of dihedral scattering components at P-band will be analyzed in sec. 4.

3.3. Hybrid decomposition technique

For separating the total P-band SAR signal into individual scattering components, the hybrid decomposition method from (Fluhrer et al., 2022) is employed. However, instead of using the extracted soil scattering component for soil moisture estimation as in (Fluhrer et al., 2022), the focus is on the dihedral scattering component for analyzing the potential to estimate trunk permittivity.

As described in (Fluhrer et al., 2022), the polarimetric coherency matrix $[T]$, based on co- and cross-polarized SAR signals, is decomposed into the three individual components of surface $[T_s]$, dihedral $[T_d]$ and volume $[T_v]$ scattering (Jagdhuber et al., 2015; Fluhrer et al., 2022):

$$\begin{bmatrix} T_{11} & T_{12} & T_{13} \\ T_{12}^{*} & T_{22} & T_{23} \\ T_{13}^{*} & T_{23}^{*} & T_{33} \end{bmatrix} = [T_s] + [T_d] + [T_v], \tag{11}$$

where the superscript * denotes the complex conjugate.

By assuming reflection symmetry (since pixels, where this assumption normally does not hold, such as urban or high mountain regions, are not analyzed in this study), we can solve for soil and dihedral scattering components. For that, the volume scattering component $[T_v]$ is subtracted from $[T]$, calculated based on the particle anisotropy (A_p; [−]), the width of the orientation angle distribution ($\Delta\psi$; [°]), and the volume scattering intensity (f_v; [−]):

$$[T_v] = \frac{f_v}{2 + 2A_p^2} \begin{bmatrix} V_{11} & V_{12} & 0 \\ V_{12}^{*} & V_{22} & 0 \\ 0 & 0 & V_{33} \end{bmatrix}, \tag{12}$$

with the volume scattering components V_{11}, V_{12}, V_{22}, V_{33}, and f_v described in (Fluhrer et al., 2022). Since f_v is dependent on the dihedral scattering angle α_d, it is modeled with the Fresnel (Sec. 3.1.) as well as the x-Fresnel (Sec. 3.2.) model, denoted by $\alpha_d^{Fresnel}$ and $\alpha_d^{x-Fresnel}$, respectively. Finally, the dihedral scattering angle α_d^{SAR} and intensity f_d^{SAR} can be estimated from the total SAR signal (Fluhrer et al., 2022).

In this study, we employ the decomposition method twice, once based on the Fresnel model, and again based on the x-Fresnel model. In sec. 4., we are analyzing, which model is most suited for P-band analyses.

3.4. Retrieval approach for trunk moisture

For final trunk permittivity estimation, a non-iterative approach is used with realistic ranges for input permittivity values. Since α_d^{Model} is used as input for the separation of the total SAR signal, a directory of α_d^{Model} and f_d^{Model} for every $\varepsilon_t \in [2, 60]$ is created (Sec. 3.1. & 3.2.). The final ε_t is then estimated from the best fit between modeled (α_d^{Model}; f_d^{Model}) and data-based components (α_d^{SAR}; f_d^{SAR}):

$$\varepsilon_t = min\left(\left|\alpha_d^{SAR} - \alpha_d^{Model}\right| + \left|f_d^{SAR} - f_d^{Model}\right|\right), \tag{13}$$

with $Model \in$ [Fresnel, x-Fresnel].

In theory, it is possible to retrieve soil and trunk moisture simultaneously from this approach. However, we decided to use in-situ measured soil moisture measurements as input during simulations since the focus is on trunk permittivity, and to reduce the computational costs as well as the retrieval complexity. For variable soil moisture inputs ranging from 6 to 40, variable trunk permittivity ranging from 2 to 60, and variable rotation limit angles ranging from 0° to 90°, we would end up with 187.915 simulations for every individual SAR pixel. This would take weeks up to months for the investigated study areas. Hence, as there are many approaches for sufficiently estimating the soil moisture from SAR remote sensing, we focus on estimating and analyzing the trunk permittivity.

4. Sensitivity study

Until now, model simulations for polarimetric scattering angle and intensity are performed with static values for important input parameters, i.e., the loss factor m_D, the phase angle φ (Sec. 3.1.), and the rotation limit angle θ_1 (Sec. 3.2.). In this section, sensitivity studies for analyzing the impact of dynamizing these model parameters are performed.

For that, we built on knowledge gained from previous studies (Weiss, 2015). investigated the influence of the local incidence angle θ_i and the vertical RMS height s on the loss factor m_D, see Figs. 6–7 in (Weiss, 2015). This study showed that for increasing θ_i, m_D decreases towards zero, while for increasing s, m_D increases from zero towards higher values. The differences in m_D-values are hereby always greater for the Gaussian ACF compared to the exponential ACF. These findings can be confirmed by sensitivity analyses shown in Fig. 2. In addition to analyzing the influence of θ_i and s on simulated m_D, we also show the influence of the employed frequency. With increasing frequency (from P- to C-band), lower m_D values are estimated at already lower surface roughness values. This is in line with previous studies which showed less influence of surface roughness at P-band wavelengths (Shen et al., 2022; Ulaby and Long, 2014). However, since at P-band, m_D is still varying between 0.4 and 1, depending on the incidence angle and surface roughness (Fig. 2, first row), we are calculating m_D for every SAR pixel individually. For one, we are using the AirMOSS incidence angle as input. Second, similar to the previous study from (Fluhrer et al., 2022), we are fixing s for every individual SAR pixel based on TanDEM-X derived surface roughness indicators (Tab. 3 in (Fluhrer et al., 2022)), to account for surface irregularities due to roughness. Lastly, we are focusing on the exponential loss factor m_D^{expo} (Eq. (5)), since differences are not that significant but to save computational costs.

Further (Weiss, 2015), investigated the relationship between modeled Fresnel parameters, $\alpha_d^{Fresnel}$ and $f_d^{Fresnel}$ (Eqs. (3) and (4), Sec. 3.1.), and varying θ_i as well as increasing soil ε_s and trunk ε_t permittivity. It can be noticed that for θ_i smaller than 45°, $\alpha_d^{Fresnel}$ is mainly a function of ε_t, while $f_d^{Fresnel}$ is mainly a function of ε_s. For θ_i greater than 45°, the relation of the scattering angle and intensity is reversed, respectively. At θ_i equal to 45°, the relation between $\alpha_d^{Fresnel}$ and $f_d^{Fresnel}$ is linear and both parameters are function of both permittivity inputs (Fig. 9 in (Weiss, 2015)).

Similar to the study of (Weiss, 2015) for the Fresnel parameters, the same behavior can be confirmed also for the x-Fresnel parameters (Fig. 3). However, besides θ_i, also the phase angle influences the relationship of $\alpha_d^{x-Fresnel}$ and $f_d^{x-Fresnel}$ across varying permittivity (Fig. 3). As mentioned before, φ is set to 0° in previous studies (Weiss, 2015; Jagdhuber, 2016), since the assumption of negligible propagation in oriented vegetation makes it unnecessary to account for phase differences between horizontal and vertical polarized backscatters. For non-oriented vegetation and at P-band however, this assumption can lead to an overestimation of model parameters, as shown in Fig. 3. It can be seen that for increasing φ, meaning increasing phase differences between horizontal and vertical polarized backscatters, overall lower $\alpha_d^{x-Fresnel}$ and higher $f_d^{x-Fresnel}$ values are reached. At $\varphi = 0°$, $\alpha_d^{x-Fresnel}$ varies between 102° and 130° and $f_d^{x-Fresnel}$ varies between 0.02 and 0.6 (Fig. 3, first row). In contrast, when accounting for highest possible phase differences between backscatters ($\varphi = 90°$), the simulated dihedral scattering parameters vary in a much broader value range ($\alpha_d^{x-Fresnel}$ between 62° and 116°, $f_d^{x-Fresnel}$ between 0.02 and 4.4). Although, the influence of φ is reported here only for the x-Fresnel model parameters, the same influence can be stated for the Fresnel model parameters.

Due to the significant influence of φ on model parameters, we are calculating φ for every analyzed SAR pixel individually in this study, based on the recorded SAR observations:

$$\varphi = \left|tan^{-1}\left(\frac{\langle S_{HH}S_{VV}^{*}\rangle''^{2}}{\langle S_{HH}S_{VV}^{*}\rangle'^{2}}\right)\right|, \tag{14}$$

where $\langle S_{HH}S_{VV}^{*}\rangle'$ is the real part and $\langle S_{HH}S_{VV}^{*}\rangle''$ is the imaginary part of the $\langle S_{HH}S_{VV}^{*}\rangle$ phase information. '⟨⟩ denotes spatial ensemble average in the data processing' (Alemohammad et al., 2018).

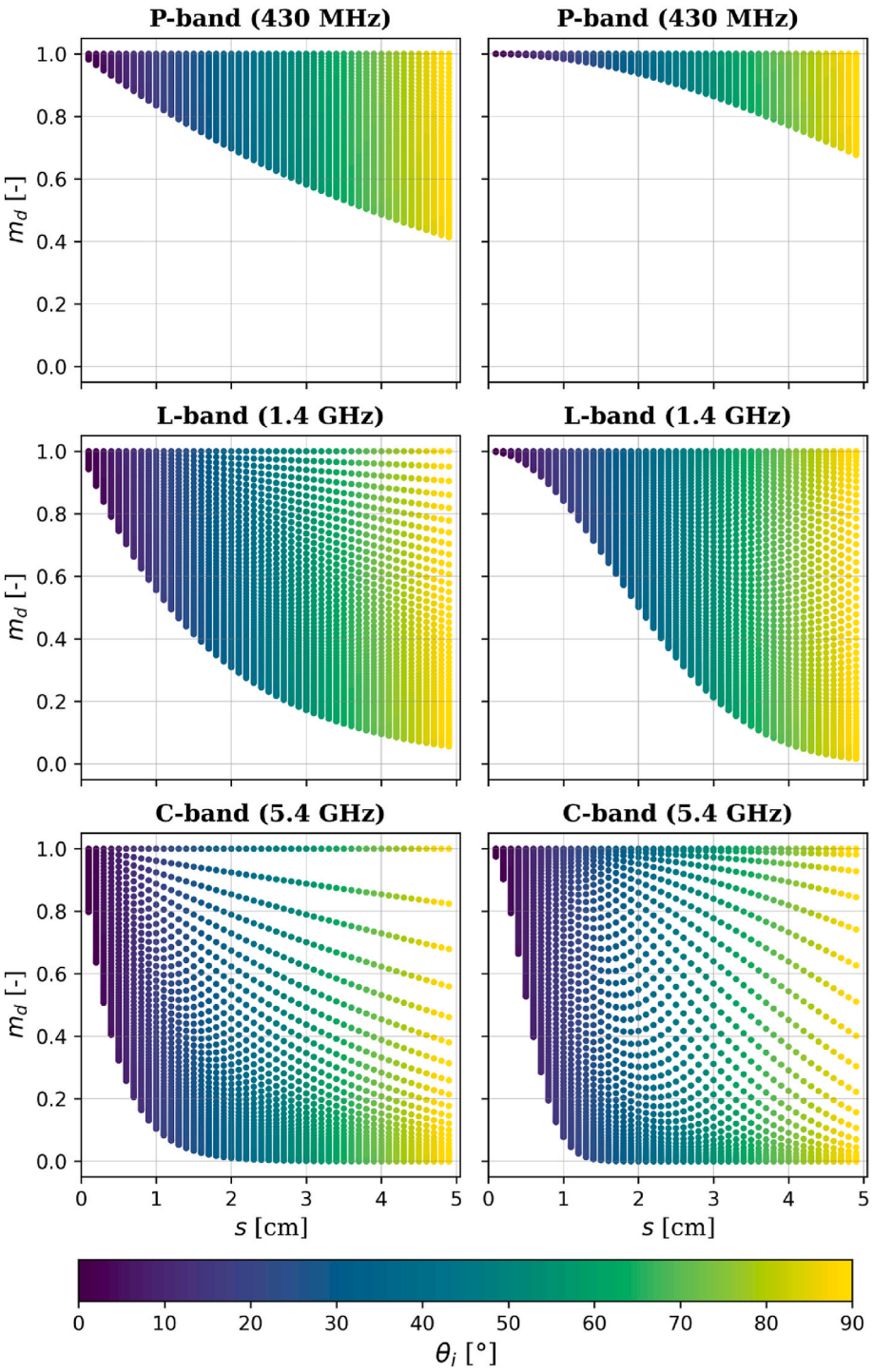

Fig. 2. Sensitivity of the simulated loss factor m_D on the vertical surface roughness parameter $s \in [0, 5]$ *cm* and the incidence angle $\theta_i \in [0, 90]^\circ$ for varying frequencies from P- to C-band. Left column: exponential ACF (Eq. (5)); right column: Gaussian ACF (Eq. (6)).

Lastly (Jagdhuber, 2016), investigated the influence of the rotation limit angle θ_1 on the x-Fresnel scattering components T_{12}^D and T_{22}^D (Eqs. (9) and (10), Sec. 3.2.) for varying θ_i and ε_t. Overall, this study could show only minor impacts with differences smaller than 3 dB between $\theta_1 = 0^\circ$ and $\theta_1 = 90^\circ$ (Figs. 2–4 in (Jagdhuber, 2016)). Further, this study investigated the relation of θ_1 and $\alpha_d^{x-Fresnel}$ for varying θ_i and showed that the simulated $\alpha_d^{x-Fresnel}$ varies between $\sim 5^\circ$ and 40° depending on θ_1 and θ_i (Fig. 26 in (Jagdhuber, 2016)). Generally, $\alpha_d^{x-Fresnel}$ increases across all investigated θ_i for increasing θ_1 between 0° and 50° and decreases for θ_1 greater than 50°. The highest variability and strongest decrease in $\alpha_d^{x-Fresnel}$ values along θ_1 is estimated for the smallest θ_i of 30°. In Fig. 4, the same behavior of simulated $\alpha_d^{x-Fresnel}$ can be seen along increasing θ_1. In addition, we investigated the influence of variable permittivity input on simulations. As shown, $\alpha_d^{x-Fresnel}$ decreases for increasing ε_s and ε_t. Hereby, the influence of ε_t is greater compared to ε_s since the decrease in $\alpha_d^{x-Fresnel}$ values is greater at increasing ε_t (Fig. 4A and B).

Complementary, the simulation results for $f_d^{x-Fresnel}$ are shown. Overall, $f_d^{x-Fresnel}$ decreases for θ_1 angles between 0° and 65° and then

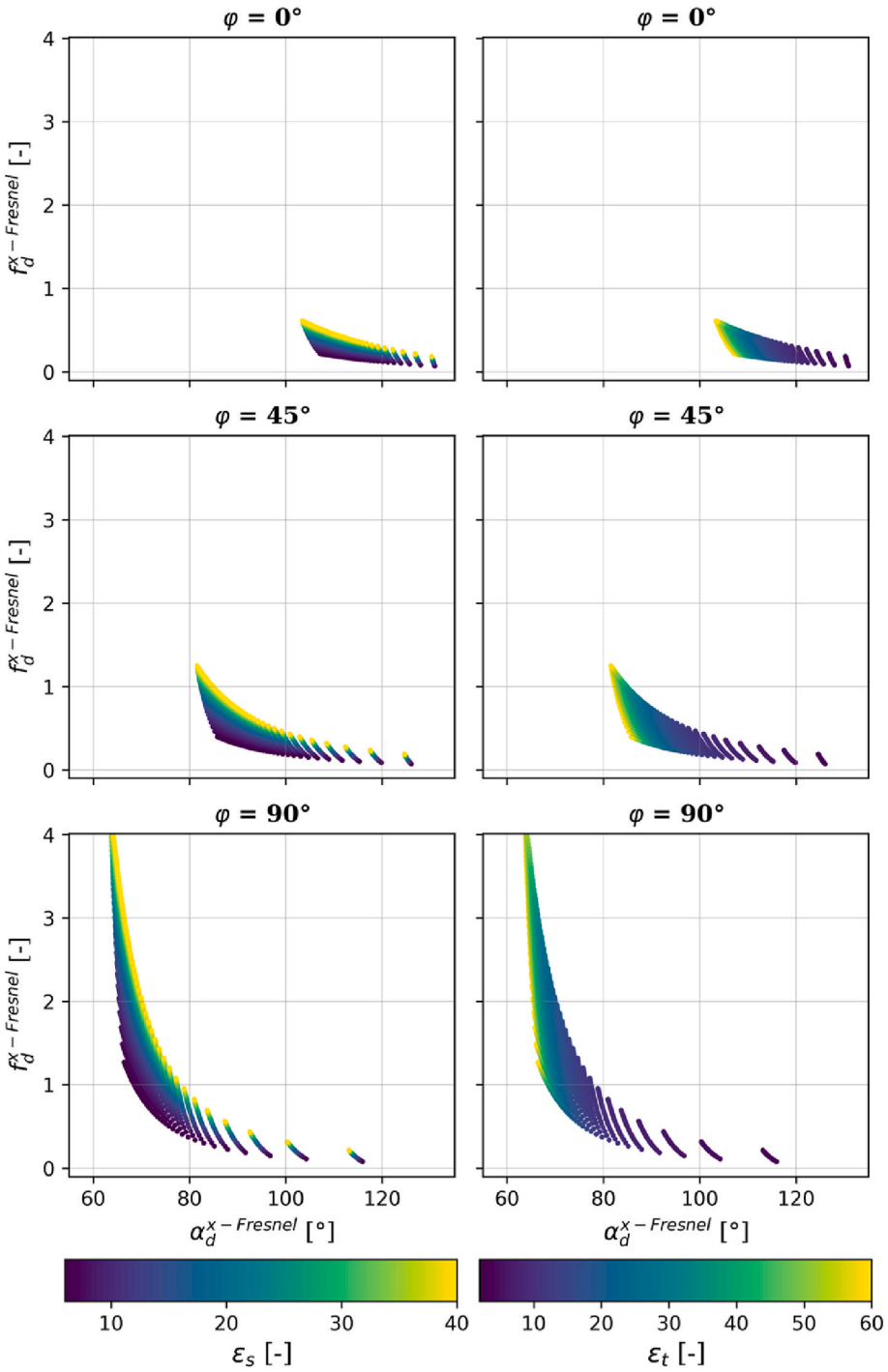

Fig. 3. Sensitivity of the simulated dihedral scattering angle $\alpha_d^{x-Fresnel}$ and intensity $f_d^{x-Fresnel}$ on the soil ($\varepsilon_s \in [6,40]$) and trunk ($\varepsilon_t \in [2,60]$) permittivity as well as the phase angle $\varphi \in [0,45,90]^\circ$. In this example, $f = 430\ MHz$, $\theta_i = 30^\circ$, $m_d = 1$, and $\theta_1 = 0^\circ$.

slightly increases until $\theta_1 = 90^\circ$. Further, $f_d^{x-Fresnel}$ increases with increasing soil and trunk permittivity, with higher decrease in $f_d^{x-Fresnel}$ at higher permittivity. The influence of both permittivity inputs on $f_d^{x-Fresnel}$ is rather minor, since value ranges are comparable for increasing ε_s and ε_t (Fig. 4C and D). In this Fig. 4, simulations are only shown for discrete permittivity values (ε_s and ε_t) due to visualization limitations. Overall, when analyzing all possible permittivity input values with $\varepsilon_s \in [6,40]$ and $\varepsilon_t \in [2,60]$ at one step, the same patterns can be reported but at different value levels, with $\alpha_d^{x-Fresnel}$ varying in total between 36.8° and 131.2°, and $f_d^{x-Fresnel}$ between 0.01 and 0.6. This means, θ_1, ε_s and ε_t have significant influence on the simulation performances of $\alpha_d^{x-Fresnel}$ and $f_d^{x-Fresnel}$. In summary it can be stated, that neglecting potential depolarization due to surface roughness is insufficient since varying θ_1 lead to different simulation results. Hence, in this study, variable values for θ_1 with $\theta_1 \in [0,90]^\circ$ are employed.

Based on the findings of conducted sensitivity studies (Figs. 2–4), we found that all three in previous studies neglected input parameters (m_D, φ, and θ_1), next to permittivity variations (ε_s, ε_t), have significant impact on modeling results. However, accounting for all three parameters, especially for depolarization effect due to soil surface roughness, is only possible with the x-Fresnel model and not with the standard Fresnel

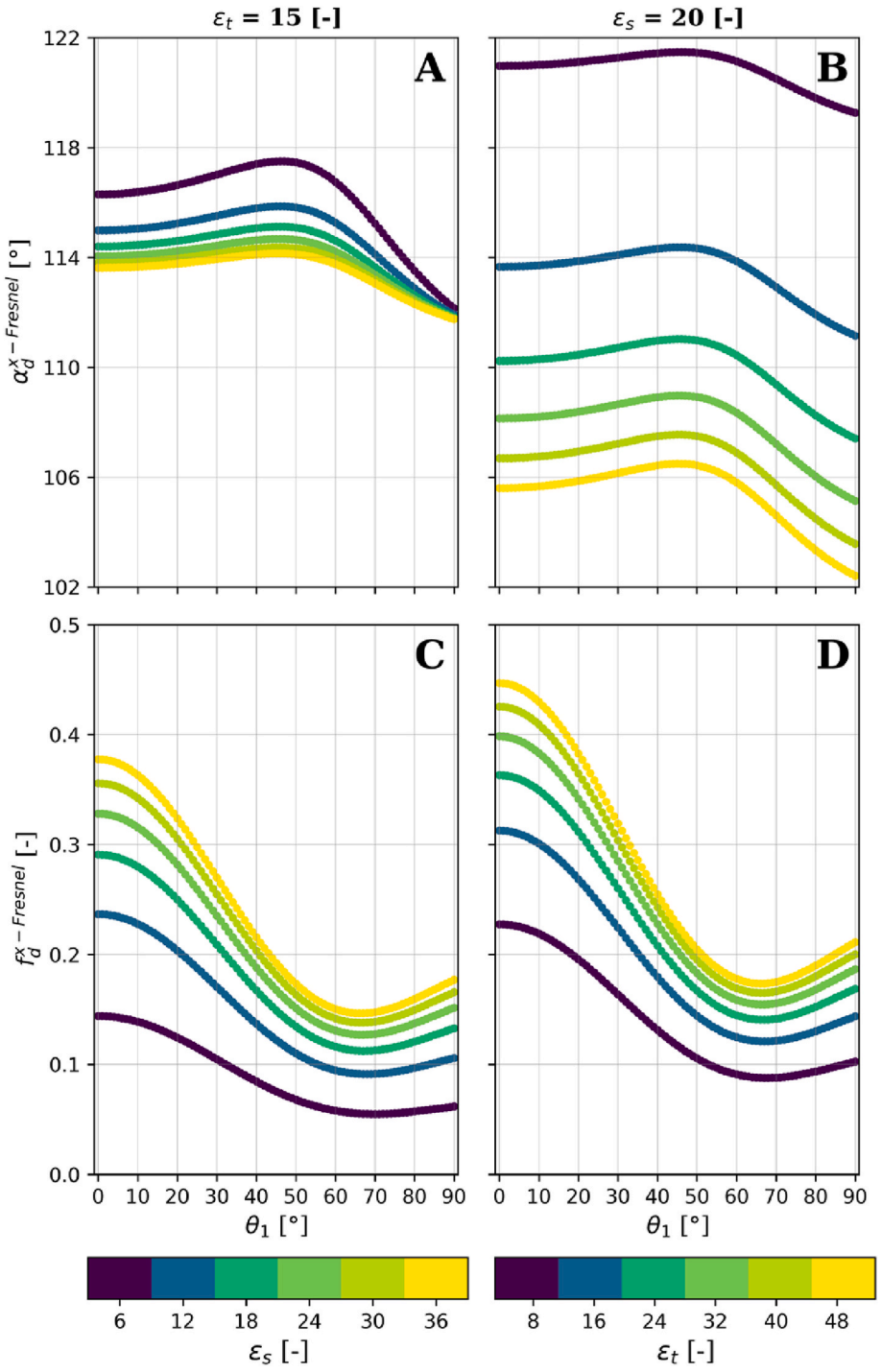

Fig. 4. Sensitivity of the simulated dihedral scattering angle $\alpha_d^{x-Fresnel}$ and intensity $f_d^{x-Fresnel}$ on the rotation limit angle θ_1 [°] and the soil ε_s and trunk ε_t permittivity. In this example, $\theta_i = 30°$, $m_d = 1$, and $\varphi = 0°$. (A) Results for $\alpha_d^{x-Fresnel}$ with $\varepsilon_t = 15$ and $\varepsilon_s \in [6,36]$. (B) Results for $\alpha_d^{x-Fresnel}$ with $\varepsilon_s = 20$ and $\varepsilon_t \in [8,48]$. (C) Results for $f_d^{x-Fresnel}$ with $\varepsilon_t = 15$ and $\varepsilon_s \in [6,36]$. (D) Results for $f_d^{x-Fresnel}$ with $\varepsilon_s = 20$ and $\varepsilon_t \in [8,48]$.

model. Hence, in the following section, only results based on the x-Fresnel model are shown and analyzed.

5. Results

5.1. Analyses regarding x-Fresnel modeling parameters

In Fig. 5, the three important input parameters, whose influence on the x-Fresnel model simulations were analyzed in detail in sec. 4., are compared to the resulting trunk permittivity for all AirMOSS monitoring dates and stations. The loss factor m_D^{expo} and phase angle φ were hereby calculated for every analyzed SAR pixel individually based on equations (5) and (14). For simulations, the rotation limit angle θ_1 was kept variable in the range $\theta_1 \in [0, 90]°$, and based on the best fit between simulations and SAR estimates, the corresponding θ_1 is shown. Significance tests between all corresponding variables in Fig. 5 revealed p-values varying between ~0 and 0.0029. Since the p-values of a two-sided Wilcoxon rank-sum test indicate the acceptance (>0.05) or rejection (<0.05) of the null hypothesis regarding continuous

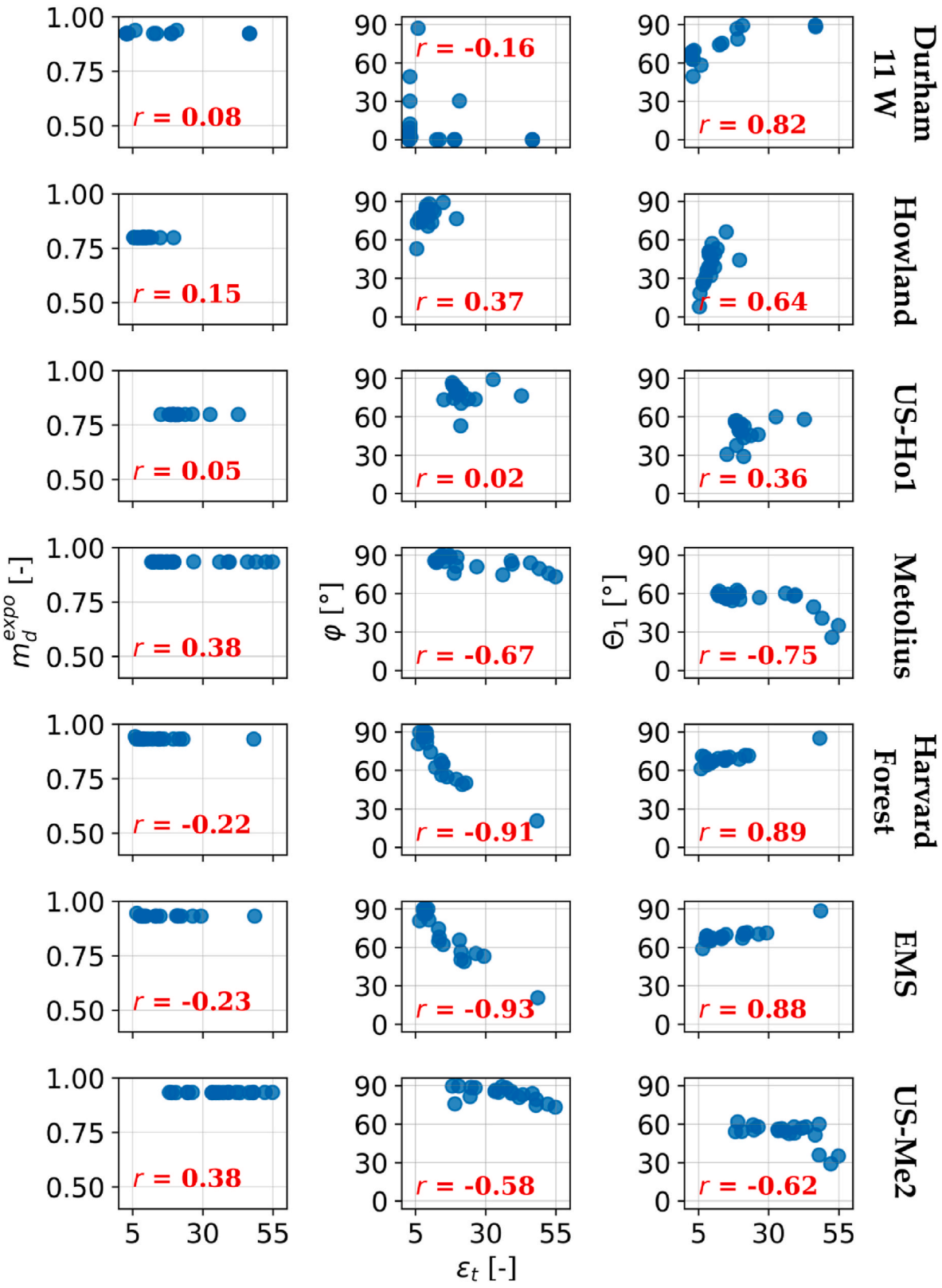

Fig. 5. Comparison of estimated trunk permittivity ε_t [−] with respective loss factor m_D^{expo} [−] (see Eq. (5)), phase angle φ [°] (see Eq. (14)), and rotation limit angle θ_1 [°] at all measuring stations and dates, except US-Me6. The red numbers give the Pearson's correlation coefficient r between two variables, respectively.

distributions with equal medians at the 5 % significance level, the displayed results can be regarded as significant.

Since m_D^{expo} is calculated from given surface roughness and AirMOSS incidence angles (Eq. (5)), which are almost the same across all dates at one respective station, it does not vary significantly within one station for multiple dates with varying ε_t, only when comparing different stations. Further, since the Pearson's correlation coefficients (r) vary in total between 0.05 and 0.38 or −0.22, no significant correlation

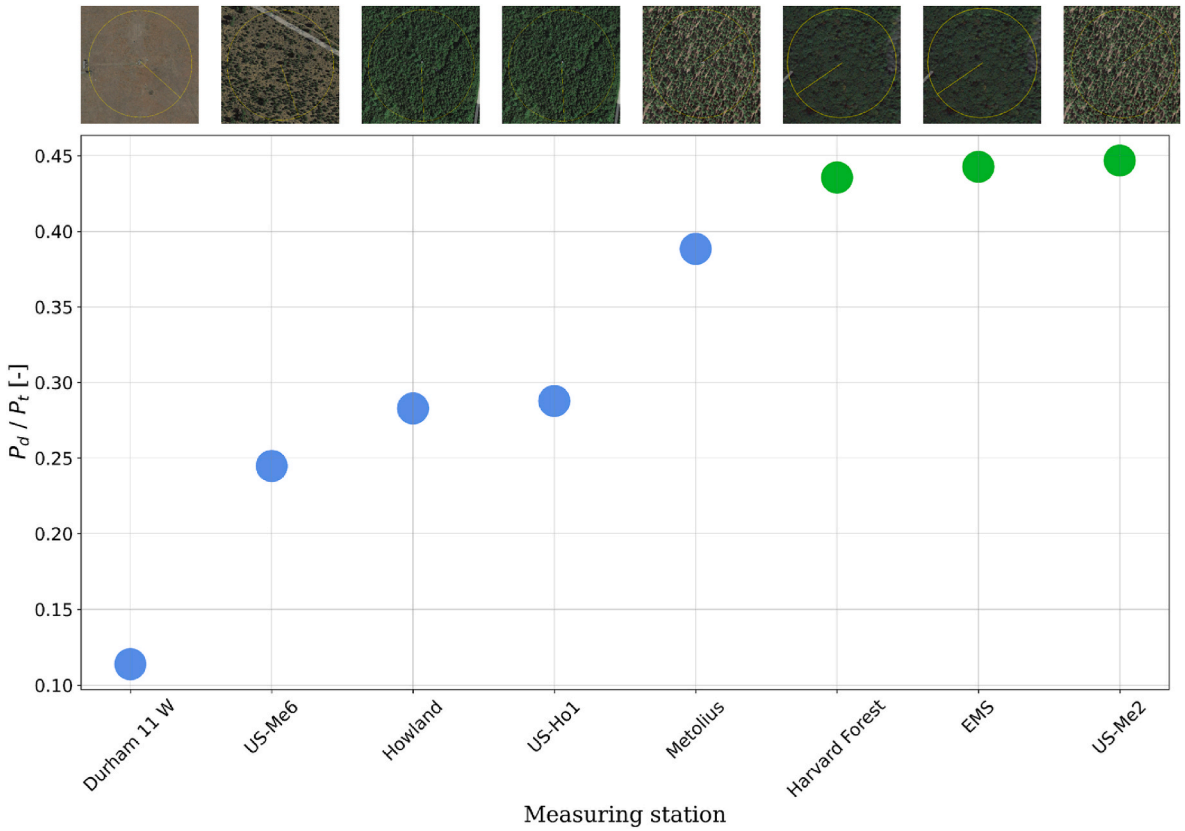

Fig. 6. Estimated normalized dihedral scattering component P_d/P_t [−] at all measuring stations with indication on vegetation cover within each SAR footprint above. Blue dots: P_d/P_t is not the dominant scattering mechanism within the P-band SAR signal. Green dots: P_d/P_t is the dominant scattering mechanism within the P-band SAR signal. Optical images on the top are from Google Earth Pro© (Fig. 1).

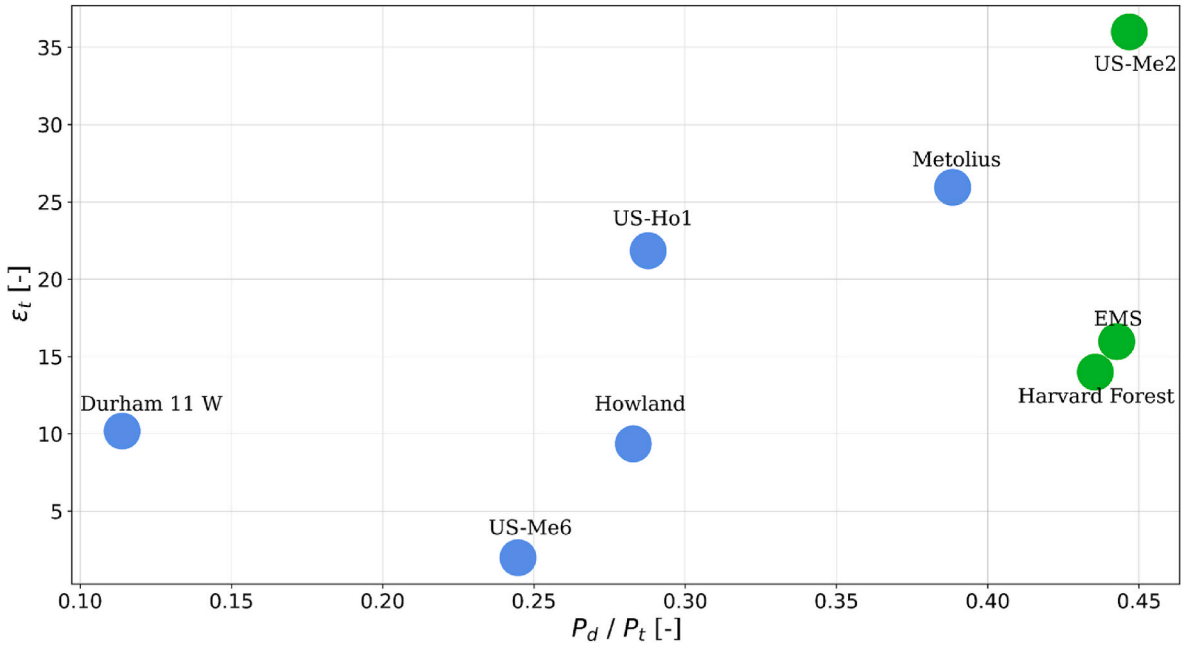

Fig. 7. The average normalized dihedral scattering component P_d/P_t [−] against the average trunk permittivity ε_t [−] for each station. Blue dots: P_d/P_t is not the dominant scattering mechanism within the P-band SAR signal. Green dots: P_d/P_t is the dominant scattering mechanism within the P-band SAR signal (from Fig. 6).

between estimated trunk permittivity and m_D^{expo} can be confirmed. At all stations, m_D^{expo} values around 0.95 are calculated, except at AirMOSS monitoring site Howland, where both stations (Howland, US-Ho1) show m_D^{expo} values around 0.8. These are also the two stations with the overall smallest estimated ε_t range across all dates and the lowest correlations (except for Durham 11 W) with $r = 0.15$ and $r = 0.05$, respectively. While at station Howland, the smallest ε_t range with values between 5.4

and 19.6 is estimated, station US-Ho1 shows values between 15.07 and 42.7. The overall highest ε_t values are estimated at station US-Me2, varying between 18.1 and 54.8. The highest r of 0.38 are estimated at both Metolius sites (Fig. 5, left column).

For calculated φ, values across the entire possible range from 0° to 90° are found at the non-forested station Durham 11 W with low correlation between φ and ε_t of $r = -0.16$. At both Howland stations (Howland, US-Ho1) φ varies between 50° and 90°, at both Metolius stations (Metolius, US-Me2) between 69° and 90°, and at both Harvard Forest stations (Harvard Forest, EMS) φ values between 51° and 90° are mainly estimated, with respectively one date at $\varphi = 22°$ showing the highest ε_t of 48 at these two stations. The latter two stations at Harvard Forest are also the stations showing the highest correlations between φ and ε_t with $r = -0.91$ and $r = -0.93$. While at all stations, an overall negative correlation can be found with increasing trunk permittivity at decreasing φ, a positive correlation is found at Howland ($r = 0.37$) and no correlation at US-Ho1 ($r = 0.02$) (Fig. 5, middle column). These are the two stations with the lowest dihedral scattering component after the non-forested station Durham 11 W (Fig. 6).

Lastly, the respectively highest correlations at every station can be found between estimated ε_t and the rotation limit angles θ_1 (except for both Harvard Forest stations, where the correlation between ε_t and φ is slightly higher). θ_1 varies between 48° and 90° at Durham 11 W, between 6° and 68° at Howland, 20°–65° at both Metolius stations (Metolius, US-Me2), and 57°–90° at both Harvard Forest stations (Harvard Forest, EMS). The lowest range of θ_1 values can be found at US-Ho1, varying between 29° and 60.1°. At all stations, a positive correlation of $r > 0.36$, meaning increasing trunk permittivity for increasing θ_1, is found except at the both rather sparsely vegetated stations (Metolius, US-Me2) of the AirMOSS monitoring site Metolius in Oregon, where high negative correlation of $r = -0.75$ and $r = -0.62$ are found (Fig. 5, right column).

5.2. Analyses regarding decomposed dihedral scattering component

For analyzing the decomposition results, we are using the relative indices of soil (P_s), dihedral (P_d), and volume (P_v) scattering normalized to the total SAR signal (P_t), which can be calculated from decomposed scattering angles and intensities (Alemohammad et al., 2018; Fluhrer et al., 2022). In Fig. 6, the estimated average normalized dihedral scattering component (P_d/P_t) is shown for all measuring stations, sorted from lowest to highest P_d/P_t. The blue dots represent stations, where the dihedral scattering component is not the dominant scattering mechanism in the SAR signal. Here, soil (P_s/P_t) or vegetation (P_v/P_t) scattering is dominating the total P-band SAR signal. Green dots give the stations, where the dihedral scattering component is the dominant scattering mechanism, namely Harvard Forest, EMS, and US-Me2. At these stations, P_d/P_t is also highest compared to all other stations, ranging around 0.44. At station Metolius, the highest value of the non-dihedral dominated stations can be found with $P_d/P_t = 0.39$, which is a bit lower compared to average P_v/P_t of 0.57. At all other stations, P_d/P_t below 0.3 are estimated, with the lowest value at Durham 11 W at 0.11, which is also is the only station where no forest appears and serves as control station. Overall, the results match with the approximate vegetation cover within every SAR footprint, since P_d/P_t approximately increases with increasing forest density around each station. Only at the two Howland Forest stations, namely Howland and US-Ho1, P_d/P_t is lower than expected, since these are located within a dense boreal broad-leaf forest.

In order to get an idea about the resulting trunk permittivity at every station, the average P_d/P_t is compared to the average estimated ε_t at every station in Fig. 7. It can be seen that the lowest ε_t of two can be found at the station US-Me6, which has the 2nd lowest P_d/P_t due to the very sparsely vegetated SAR pixel (Fig. 1). At this station, ε_t is a constant of two across all dates indicating that the method is not applicable, and hence, will be excluded in further analyses. The highest average ε_t of 36 is found at the station with highest P_d/P_t, namely US-Me2. However, the other two stations with dominant dihedral scattering, Harvard Forest and EMS, show significantly lower permittivity results around 15 than US-Ho1 (21.8) and Metolius (25.9). In contrast, the station with the lowest P_d/P_t (Durham 11 W) gives the third lowest ε_t of 10.2. Hence, the amount of dihedral scattering within the total SAR signal is not directly linked to the trunk permittivity. This is not surprising as the employed method builds not only on intensity (f_d) but also mechanism (α_d) (Sec. 3.).

5.3. Analysing results with SPAS variables at US-Me2

In Fig. 8, the daily averaged time series of in-situ measured T_{air} and RH, ET from MODIS, as well as RWC from AMSR2 (Sec. 2.) are shown for the period from March 2013 to October 2015. In addition, the in-situ measured ε_s, which is used as input for the x-Fresnel model simulations, and the estimated ε_t are displayed for the respective AirMOSS monitoring dates, where SAR measurements were recorded during the campaign. The time series is shown here only for station US-Me2, since this is the station with the highest average P_d/P_t.

Across the entire period, seasonal patterns are visible with T_{air}, ET and RWC showing highest values during summer months and lowest during winter months, with RH showing the opposite trend. Overall, there is a slight increase in the yearly averages from 2013 to 2015 in T_{air} of 0.9° and RWC of 0.93 %, and decrease in yearly averages in RH of 0.96 %, and ET of 0.04 mm/8days. Meaning, it is getting a bit warmer with slightly increasing RWC and decreasing RH and ET. The in-situ measured ε_s shows no clear trend with in average lowest values in 2014 (6.1) compared to 2013 (8.7) and 2015 (7.2). The estimated ε_t however, also shows a decreasing trend in yearly averages from 45.6 in 2013 to 29.3 in 2015.

More detailed analyses at specific dates indicate the in general good agreement between estimated ε_t and environmental conditions. It seems that, in general, estimated ε_t is positively correlated with RWC, ET, and RH, meaning increasing ε_t during increasing RWC, ET and RH, and negatively correlated with T_{air}, meaning decreasing ε_t during increasing T_{air}. For example, at the first three AirMOSS dates (April, 21, 25, and 29, 2013), T_{air}, ET, and RWC are increasing, while RH and ε_s are decreasing. During these first two dates, ε_t is increasing from 48 to 54.8 and then slightly decreasing to 52.1. In contrast, when T_{air}, RWC and ET are decreasing, while RH is increasing and ε_s is constant, the estimated ε_t is decreasing slightly as well from 37.3 to 35.8 (Fig. 8). The same trends can be observed at some other AirMOSS dates. However, one has always keep in mind the discrepancy in spatial resolutions between in-situ measurements (point precise), AirMOSS estimates (90 m) as well as MODIS (500 m), and AMSR2 (10 km) pixels, and the coarse temporal resolution of the AirMOSS dates (in total 20 dates in three years), which allows no time series analyses.

5.4. Analysing results with SPAS variables at selected stations

In Table 1, the statistics of estimated ε_t at evaluated stations are given. The highest average ε_t of 36 and standard deviation of 14.6 is found at the two stations (US-Me2, Metolius) within the AirMOSS monitoring site Metolius, which are the stations with the highest P_d/P_t and highest non-dominant P_d/P_t (Fig. 6). The lowest ε_t of 9.4 and standard deviation of 3.1 is found at station Howland, the station with the 2nd lowest average P_d/P_t (Fig. 6). This is also the station with the lowest range in estimated ε_t, varying from 5.5 (5 % percentile) to 14.8 (95 % percentile). The highest range in ε_t is found at station Metolius, ranging between 12.3 (5 % percentile) and 52.5 (95 % percentile), closely followed by the neighboring station US-Me2.

For more detailed analyses, the trunk permittivity results at all stations for all available AirMOSS dates are compared to auxiliary parameters in Fig. 9. For one, the stations appear in the order of their average P_d/P_t (Fig. 6) from top to bottom. Second, the scatterplots show

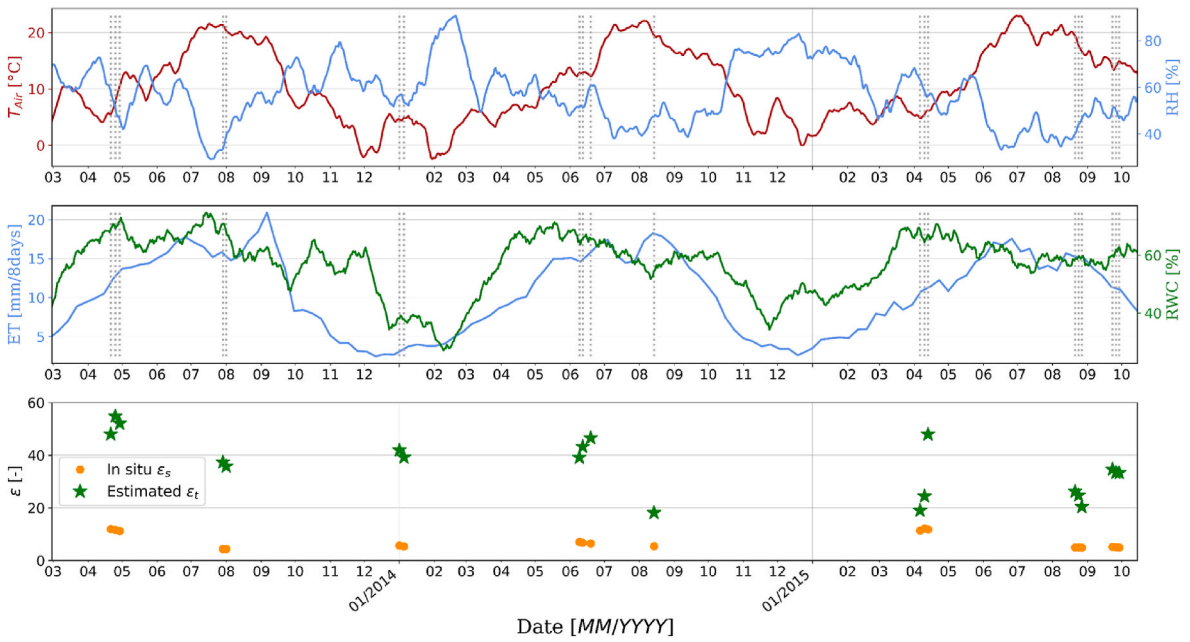

Fig. 8. Seasonal patterns of daily averaged in-situ measured air temperature (T_{air}; [°C]), relative humidity (RH; [%]), MODIS evapotranspiration (ET; [mm/8days]), and AMSR2 relative water content (RWC; [%]) for the period 2013–2015 together with in-situ measured soil permittivity (ε_s; [−]) and estimated trunk permittivity (ε_t; [−]) at AirMOSS measuring dates of station US-Me2, Metolius, OR. The time series of T_{air}, RH, and RWC are cleaned for daily dynamics using the Savitzgy-Golay filter with a window size of 21 (days), the MODIS ET time series with a window size of three (21 days). Dashed grey lines in the first two subplots indicate the dates of available AirMOSS measurements.

the comparison of RWC (1st column), ET (2nd column), RH (3rd column), and T_{air} (4th column) with estimated ε_t. The colors indicate the amount of P_d/P_t for every AirMOSS date.

In general, with increasing P_d/P_t, meaning higher portion of dihedral scattering in the total SAR signal, Pearson's correlation coefficient r is increasing as well. Further, a positive correlation is observable between ε_t and RWC, ET, and RH, while T_{air} is negatively correlated with ε_t. These trends can be mostly observed at the stations, where the P_d/P_t is dominant in the total SAR signal and at Metolius, which is the one with the highest P_d/P_t of the non-dihedral dominated stations (Fig. 6). The latter is also the station which gives almost always the highest r. Here, the respectively highest r can be found between ε_t with RWC of 0.47, ET of 0.6, and RH of 0.31. Only in comparison with T_{air}, the r of −0.31 is lower than the one at station US-Ho1 with r = -0.58. For individual dates, no clear pattern regarding the amount of P_d/P_t and estimated ε_t can be found. In general, realistic ε_t are estimated for higher P_d/P_t but the trend that can be observed from these analyses is nonlinear. First reason is that not only intensity plays a role in the employed method (f_d) but also mechanism (α_d) (Sec. 3.). Second reason is that a certain amount of dihedral scattering, coming from soil-stem interactions, is necessary in the first place in order for the method to be applicable and produce realistic ε_t.

6. Discussion

The proposed retrieval method incorporates the x-Fresnel scattering model, which showed to be most appropriate when decomposing P-band SAR signals for trunk permittivity estimation (sec. 4.). It could be demonstrated that the model is sensitive to input parameters that are kept constant in previous studies, the loss factor m_D, the phase angle φ (sec. 3.1.), and the rotation limit angle θ_1 (sec. 3.2.). m_D accounts for scattering losses at the soil plane on the dihedral scattering intensity and is set to one in previous studies (Jagdhuber, 2016). However, detailed sensitivity analyses in this study revealed that m_D should be calculated for every SAR signal individually depending on the given surface roughness and local incidence angle in order to reflect natural, lossy surfaces with changing surface roughness. Final results for individual SAR pixels across boreal transitional or mixed as well as temperate evergreen needle-leaf forests in the U.S. (Sec. 2.) showed that m_D varies between 0.8 and 0.95 (Fig. 5). A fixed m_D of one would have led to an underestimation of estimated ε_t. In future studies, the calculation of m_D can even be improved by available soil surface roughness information at high resolution, e.g. from airborne or terrestrial lidar surveys.

Further, as stated in sec. 3.1., φ expresses the phase differences between horizontal and vertical polarized backscatters. Previous studies based on L-band assumed negligible propagation in oriented vegetation, which makes it dispensable to account for phase differences and hence, used $\varphi = 0$ (Jagdhuber, 2016; Weiss, 2015). However, this assumption does not hold when using P-band SAR observations with distinct penetration and transmission capabilities into the forest canopy and can lead to an overestimation of model parameters and consequently false ε_t estimates. Here, we calculated φ for every SAR pixel and observation individually based on the complex phase information $\langle S_{HH}S_{VV}^{*}\rangle$ (Alemohammad et al., 2018). Estimated φ vary mostly in the range between 20° and 90°. Hence, a fixed value of 0° would significantly influence resulting ε_t, and potentially lead to an overestimation of simulated dihedral scattering angle $\alpha_d^{x-Fresnel}$ and intensity $f_d^{x-Fresnel}$ and hence, ε_t. Lastly, the extension of the x-Fresnel model to account for potential depolarization due to soil surface roughness, in comparison to the Fresnel model without this possibility, showed to be essential since scattering power and trunk permittivity results vary significantly for different θ_1. Results showed that θ_1 varies between the entire possible range from 0° to 90° at specific AirMOSS stations (Fig. 5). This means, a fixed θ_1 of 0°, assuming no depolarization (rotation) of the soil and trunk plane (Jagdhuber, 2016), leads to potentially erroneous ε_t estimates.

The average decomposed dihedral scattering component matches the forest conditions at all stations, with almost no contribution of dihedral scattering within the total SAR signal at the bare soil station Durham 11W (acting as control station), and highest contribution at the moderately dense temperate, evergreen needle-leaf forest station, with the most dense, homogeneously covered boreal forest stations in between. Hence, the dihedral scattering component shows sensitivity for

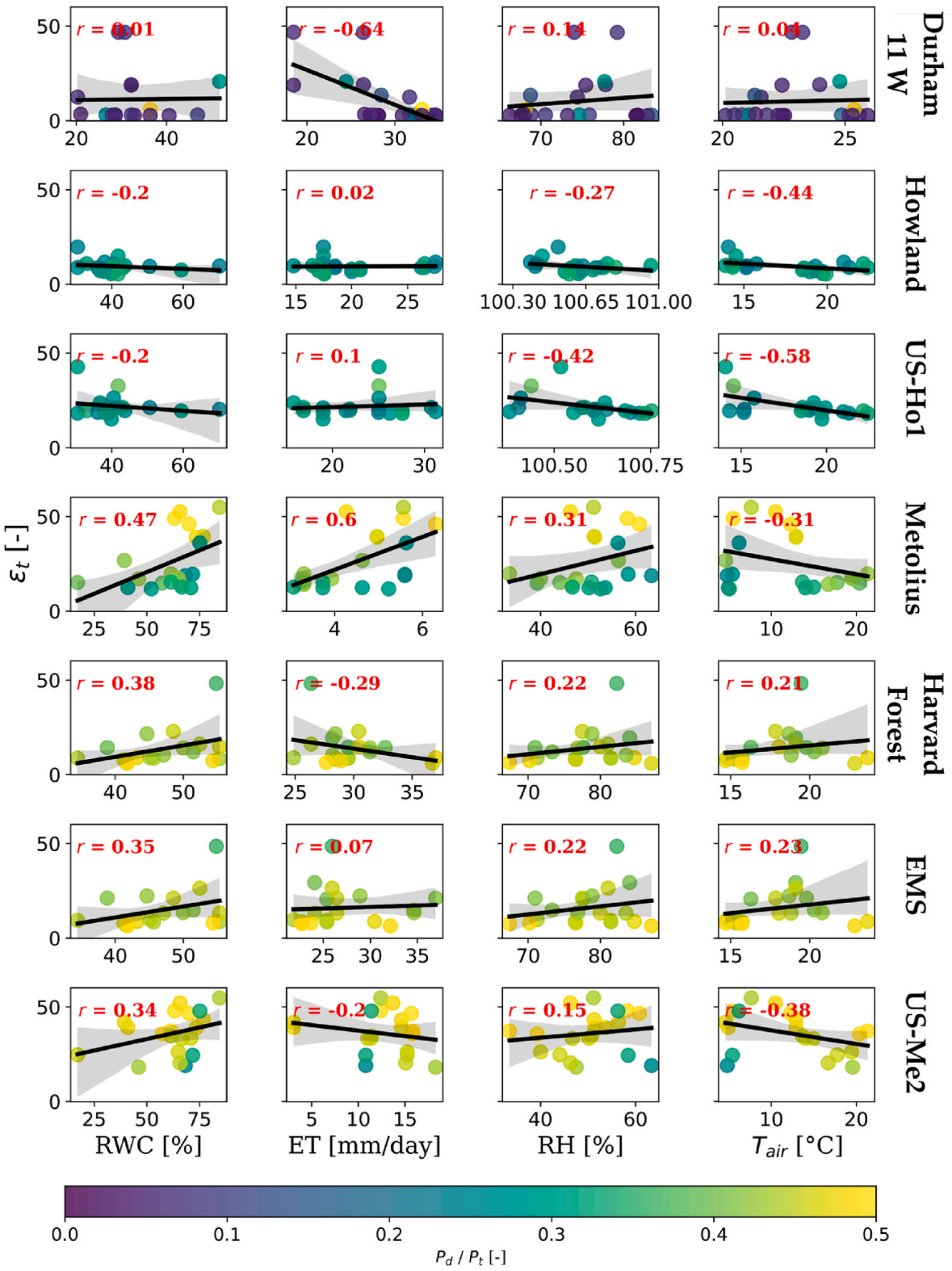

Fig. 9. Comparison of AMSR2 relative water content (RWC; [%]), MODIS evapotranspiration (ET; [mm/days]), in-situ measured relative humidity (RH; [%]), and in-situ measured air temperature (T_{air}; [°C]) with estimated trunk permittivity (ε_t; [−]) at all measuring stations, except US-Me6. The stations are sorted after the average normalized dihedral scattering component P_d/P_t from top to bottom. The color represents the amount of normalized dihedral scattering P_d/P_t [−] within the total P-band SAR signal. Black lines give the linear regression fit between respective parameters and the red numbers give the Pearson's correlation coefficient r between two variables, respectively.

Table 1
The mean, standard deviation (STD) as well as the 5 % and 95 % percentiles of estimated trunk permittivity at all measuring stations, except US-Me6. The stations are sorted after the average normalized dihedral scattering component P_d/P_t from left to right as shown in Fig. 6.

	Durham 11 W	Howland	US-Ho1	Metolius	Harvard Forest	EMS	US-Me2
Mean	10.2	9.4	21.8	25.9	14	16	36
Std	13	3.1	6.1	14.6	9.2	10	10.8
5 %	2.8	5.5	17.8	12.3	6.4	7.6	18.9
95 %	45.3	14.8	33.6	52.5	24.1	30.3	52.2

different site conditions and forest types. In general, estimated ε_t from AirMOSS P-band data varies between 2.4 and 59.7. At pixels, where the dihedral scattering mechanism is dominating the total SAR signal (Harvard Forest, EMS, and US-Me2) and station Metolius (highest average dihedral scattering component of non-dominated dihedral stations), in average higher ε_t could be estimated, ranging from 14 to 25.9 (Table 1). Here, estimated ε_t varies between the 5 % and 95 % percentile from 6.4 to 52.5 (Table 1).

This is in line with previous studies analyzing ε_t. For example (Franchois et al., 1998), presented a study conducting laboratory measurements of permittivity of two types of coniferous trees (prevalent in many forested regions) using microwave techniques for frequencies from 1 to 10 GHz. They found, that ε_t decreases with increasing frequency and reported values between 8.9 and 54.4, with generally higher values in the phloem (inner side of the bark of a trunk) and lower values in the xylem (major constituent of a trunk surrounded by cambium and bark) (Franchois et al., 1998). This means, a trunk shows increasing permittivity from the center of the trunk to the outside, which is also reported by, e.g., (Dobson et al., 1991; McDonald et al., 1999, 2002). Hence, differences in ε_t are not only influenced by atmospheric and meteorological conditions, but also the composition of individual tree trunk. Further, in the study of (McDonald et al., 2002), the authors investigated the diurnal and spatial variations of the xylem permittivity in Norway Spruce trees and its correlation with microclimate, xylem sap flow, and xylem chemistry. They found significant diurnal variations in the xylem permittivity, which were strongly correlated with changes in microclimate conditions such as temperature, humidity, and solar radiation. A similar correlation between ε_t and T_{air} as well as RH is found in this study (McDonald et al., 2002). also found spatial variations in the xylem permittivity within the tree canopy, with lower values observed at higher heights.

In summary we can state, that thicker trunks and trunks at greater heights appear rather dry compared to thinner trunks at lower heights due to the reduced penetration ability of microwaves with increasing trunk density, height, and width. This is confirmed by results shown in this study. The in average highest ε_t values are found at both stations within the AirMOSS monitoring site Metolius, which are characterized by a less dense and high temperate, evergreen needle-leaf forest. In contrast, at the monitoring site Harvard Forest, characterized by a dense boreal transitional or mixed forest, overall lower ε_t values are found. Although at station Metolius, the average dihedral scattering is not dominant in the total SAR signal, but sufficiently high (at 0.39, Fig. 6), reasonable ε_t could be estimated, even showing the highest correlations with RWC from AMSR2, ET from MODIS, and in-situ measured RH. The stations at monitoring site Howland Forest with rather low dihedral scattering proportion (in average ~0.28) show significantly lower permittivity values and almost no correlations with auxiliaries.

However, we always have to remember not only the discrepancies in spatial resolutions between in-situ measurements (point precise), AirMOSS estimates (90 m), AMSR2 (10 km), and MODIS (500 m) data, but also the differences in sensing depths and frequencies. Here, we proposed a method for ε_t estimation based on P-band SAR data (430 MHz). MODIS in contrast, retrieves ET from a simple physically-based method, the Penman-Monteith, combining remote sensing (i.e., landcover, leaf area index, albedo, etc.) from thermal or surface reflectance data with global meteorological measurements (i.e., vapor pressure deficit, RH, T_{air}, etc.) (Running et al., 2017). In addition, RWC from AMSR2 is based on observed brightness temperatures from a passive radiometer at C-band (6.925 GHz) and the Land Parameter Retrieval Model (LPRM) with underlying radiative transfer theory (Jeu and Owe, 2014; Owe et al., 2008). Thus, while the proposed approach predominantly describes ε_t and less canopy permittivity (since the dihedral scattering is used and not the volume scattering), the results are hence, not representative for the entire biomass of trees. In contrast, the RWC from AMSR2 is defined by dry biomass and the amount of water per unit biomass, describing the entire biomass and not only trunks, similar to MODIS ET, which predominantly constitutes of canopy transpiration (along with soil evaporation). The VWC is hence, correlated to the amount of biomass, which means, higher VWC occurs already with dense vegetation, as given within forests, and not only with higher vegetation moisture (Chaparro et al., 2024). This means in summary, very high correlations (e.g., >0.8) are unrealistic. However, the comparison between estimated P-band ε_t with other vegetation water content related parameters indicate apparent correlations at medium level at stations with sufficient dihedral scattering within the total SAR signal, indicating the feasibility of the proposed approach for ε_t estimation.

7. Conclusions and outlook

In this study, the decomposed dihedral scattering component of the total P-band SAR signal is analyzed to estimate trunk permittivity. The proposed hybrid decomposition method is combined with the x-Fresnel model for dihedral scattering. Within the x-Fresnel model we account, among others, for scattering losses, phase differences and depolarization effects (e.g., due to roughness) in backscatter observations. The conducted sensitivity study led to the need for the more sophisticated dihedral scattering model x-Fresnel to improve the performance of the proposed method for ε_t estimation. We focused on single SAR pixels at measuring stations, where in-situ observations are available due to missing input parameters at comparable spatial resolution to the AirMOSS data (~90 m). Results overlap with reported ε_t ranges in previous studies and are in line with site dependent environmental conditions. Results show, that thicker trunks and trunks at greater heights appear rather dry compared to thinner trunks at lower heights due to the reduced penetration ability of microwaves with increasing trunk density, height, and width. The in average highest ε_t values are found at the less dense vegetated evergreen needle-leaf forest stations (at the Metolius site) since here, as compared to more dense vegetated forests like the broad-leaf forest stations (at the Howland site), due to the clear line of sight the dihedral scattering mechanisms is stronger. Further, the evergreen needle-leaf forest stations showed clear dependencies between estimated permittivity and relative water content from AMSR2, evapotranspiration from MODIS, and in-situ measured relative humidity and air temperature. Overall, calculated correlations range between ±0.1 and ± 0.64. However, we always have to remember not only the discrepancies in spatial resolutions between in-situ measurements, AirMOSS estimates, AMSR2, and MODIS data, but also the differences in sensing depths and frequencies. Further, the proposed approach predominantly describes trunk permittivity and less canopy permittivity (since the dihedral scattering is used and not the volume scattering). Hence, the results are not representative for the entire biomass of trees, as, for example, the RWC from AMSR2 or ET from MODIS. The station

(Durham 11 W), which was used as control case, since no trees appeared within the radar footprint of this station, delivered the worst results. Here, the expected lowest amount of dihedral scattering within the total SAR signal is estimated due to the missing possibility of wave interaction between tree trunks and the soil. Hence, the lowest permittivity values are found at this station since the proposed method violates the physical boundaries.

This study demonstrated the potential of the dihedral scattering component of polarimetrically decomposed SAR signals for ε_t estimation. Future add-on studies regarding the simultaneous retrieval of soil and trunk permittivity can even extend the possibility of the proposed method. However, this is complicated due to the interdependence of soil and trunk permittivity within the dihedral scattering mechanism. Since soil moisture is used here as input to the ε_t retrieval, and no available soil moisture datasets at comparable spatial resolution (90 m) during the study period (2013–2015), an aerial determination of ε_t was not feasible within this study. However, the proposed method can be used to deliver global trunk/vegetation moisture maps at high spatial and temporal resolution when appropriate datasets will be available, as for example, with the upcoming NASA-ISRO (National Aeronautics and Space Administration, Indian Space Research Organization) Synthetic Aperture Radar (NISAR) mission (Kellogg et al., 2020) in 2024, and the future BIOMASS mission from the European Space Agency (ESA) in 2025 (Gelas et al., 2021).

CRediT authorship contribution statement

Anke Fluhrer: Writing – review & editing, Writing – original draft, Visualization, Validation, Software, Resources, Methodology, Investigation, Formal analysis, Data curation, Conceptualization. **Hamed Alemohammad:** Writing – review & editing, Supervision, Resources, Data curation. **Thomas Jagdhuber:** Writing – review & editing, Validation, Supervision, Project administration, Methodology, Investigation, Formal analysis, Conceptualization.

Declaration of competing interest

All authors declare that they have no known competing financial interests or personal relationships that could have appeared to influence the work reported in this paper.

Acknowledgements

The authors would like to thank former DLR employees Vincent Franke and Patrick Klein for compiling first analyses regarding this topic in their master theses.

Data availability

The authors do not have permission to share data.

References

Alemohammad, S.H., Konings, A.G., Jagdhuber, T., Moghaddam, M., Entekhabi, D., 2018. Characterization of vegetation and soil scattering mechanisms across different biomes using P-band SAR polarimetry. Rem. Sens. Environ. 209, 107–117. https://doi.org/10.1016/j.rse.2018.02.032.

AmeriFlux, 2022. https://ameriflux.lbl.gov. (Accessed 15 March 2022).

Arora, V., 2002. Modeling vegetation as a dynamic component in soil-vegetation-atmosphere transfer schemes and hydrological models. Rev. Geophys. 40. https://doi.org/10.1029/2001RG000103.

Bell, J.E., Palecki, M.A., Baker, C.B., Collins, W.G., Lawrimore, J.H., Leeper, R.D., Hall, M.E., Kochendorfer, J., Meyers, T.P., Wilson, T., Diamond, H.J., 2013. U.S. Climate reference network soil moisture and temperature observations. J. Hydrometeorol. 14, 977–988. https://doi.org/10.1175/JHM-D-12-0146.1.

Chaparro, D., Jagdhuber, T., Piles, M., Jonard, F., Fluhrer, A., Vall-llossera, M., Camps, A., López-Martínez, C., Fernández-Morán, R., Baur, M., Feldman, A.F., Fink, A., Entekhabi, D., 2024. Vegetation moisture estimation in the Western United States using radiometer-radar-lidar synergy. Rem. Sens. Environ. 303, 113993. https://doi.org/10.1016/j.rse.2024.113993.

Cloude, S., 2010. Polarisation: Applications in Remote Sensing, first ed. Oxford University Press, Oxford ; New York.

Didan, K., 2021. MODIS/Terra vegetation indices 16-day L3 global 250m SIN grid V061. https://doi.org/10.5067/MODIS/MOD13Q1.061.

Dobson, M.C., DeLaSierra, R., Christensen, N., 1991. Spatial and temporal variation of the microwave dielectric properties of loblolly pine trunks. In: Proceedings] IGARSS'91 Remote Sensing: Global Monitoring for Earth Management. Presented at the [IGARSS'91 Remote Sensing: Global Monitoring for Earth Management. IEEE, Espoo, Finland, pp. 1107–1110. https://doi.org/10.1109/IGARSS.1991.579264.

Fluhrer, A., Jagdhuber, T., Tabatabaeenejad, A., Alemohammad, H., Montzka, C., Friedl, P., Forootan, E., Kunstmann, H., 2022. Remote sensing of complex permittivity and penetration depth of soils using P-band SAR polarimetry. Remote Sens. 14, 2755. https://doi.org/10.3390/rs14122755.

Franchois, A., Pineiro, Y., Lang, R.H., 1998. Microwave permittivity measurements of two conifers. IEEE Trans. Geosci. Rem. Sens. 36, 1384–1395. https://doi.org/10.1109/36.718840.

Freeman, A., Durden, S.L., 1998. A three-component scattering model for polarimetric SAR data. IEEE Trans. Geosci. Rem. Sens. 36, 963–973. https://doi.org/10.1109/36.673687.

Gao, B., 1996. NDWI—a normalized difference water index for remote sensing of vegetation liquid water from space. Rem. Sens. Environ. 58, 257–266. https://doi.org/10.1016/S0034-4257(96)00067-3.

Gaulton, R., Danson, F.M., Ramirez, F.A., Gunawan, O., 2013. The potential of dual-wavelength laser scanning for estimating vegetation moisture content. Rem. Sens. Environ. 132, 32–39. https://doi.org/10.1016/j.rse.2013.01.001.

Gelas, C., Villard, L., Ferro-Famil, L., Polidori, L., Koleck, T., Daniel, S., 2021. Multi-temporal speckle filtering of polarimetric P-band SAR data over dense tropical forests: study case in French guiana for the BIOMASS mission. Remote Sens. 13, 142. https://doi.org/10.3390/rs13010142.

Gu, Y., Hunt, E., Wardlow, B., Basara, J.B., Brown, J.F., Verdin, J.P., 2008. Evaluation of MODIS NDVI and NDWI for vegetation drought monitoring using Oklahoma Mesonet soil moisture data. Geophys. Res. Lett. 35, 2008GL035772. https://doi.org/10.1029/2008GL035772.

He, L., Panciera, R., Tanase, M.A., Walker, J.P., Qin, Q., 2016. Soil moisture retrieval in agricultural fields using adaptive model-based polarimetric decomposition of SAR data. IEEE Trans. Geosci. Rem. Sens. 54, 4445–4460. https://doi.org/10.1109/TGRS.2016.2542214.

Homeland Infrastructure Foundation-Level Data (HIFLD), 2012. Political boundaries. https://hifld-geoplatform.opendata.arcgis.com/. (Accessed 24 June 2019).

Jagdhuber, T., 2016. An approach to extended Fresnel scattering for modeling of depolarizing soil-trunk double-bounce scattering. Remote Sens. 8, 818. https://doi.org/10.3390/rs8100818.

Jagdhuber, T., Hajnsek, I., Papathanassiou, K.P., 2015. An iterative generalized hybrid decomposition for soil moisture retrieval under vegetation cover using fully polarimetric SAR. IEEE J. Sel. Top. Appl. Earth Obs. Rem. Sens. 8, 3911–3922. https://doi.org/10.1109/JSTARS.2014.2371468.

Jeu, R. de, Owe, M., 2014. AMSR2/GCOM-W1 surface soil moisture (LPRM) L3 1 day 10 km x 10 km ascending V001. Goddard Earth Sciences Data and Information Services Center (GES DISC) (Bill Teng), Greenbelt, MD, USA, Goddard Earth Sciences Data and Information Services Center (GES DISC). https://doi.org/10.5067/B0GHODHJLDA8 [Data set]. (Accessed 2 November 2022).

Kellogg, K., Hoffman, P., Standley, S., Shaffer, S., Rosen, P., Edelstein, W., Dunn, C., Baker, C., Barela, P., Shen, Y., Guerrero, A.M., Xaypraseuth, P., Sagi, V.R., Sreekantha, C.V., Harinath, N., Kumar, R., Bhan, R., Sarma, C.V.H.S., 2020. NASA-ISRO synthetic aperture radar (NISAR) mission. In: 2020 IEEE Aerospace Conference. Presented at the 2020 IEEE Aerospace Conference. Big Sky, IEEE, pp. 1–21. https://doi.org/10.1109/AERO47225.2020.9172638. MT, USA.

Kim, Yihyun, Jackson, T., Bindlish, R., Lee, Hoonyol, Hong, Sukyoung, 2012. Radar vegetation index for estimating the vegetation water content of rice and soybean. Geosci. Rem. Sens. Lett. IEEE 9, 564–568. https://doi.org/10.1109/LGRS.2011.2174772.

Konings, A.G., Saatchi, S.S., Frankenberg, C., Keller, M., Leshyk, V., Anderegg, W.R.L., Humphrey, V., Matheny, A.M., Trugman, A., Sack, L., Agee, E., Barnes, M.L., Binks, O., Cawse-Nicholson, K., Christoffersen, B.O., Entekhabi, D., Gentine, P., Holtzman, N.M., Katul, G.G., Liu, Y., Longo, M., Martinez-Vilalta, J., McDowell, N., Meir, P., Mencuccini, M., Mrad, A., Novick, K.A., Oliveira, R.S., Siqueira, P., Steele-Dunne, S.C., Thompson, D.R., Wang, Y., Wehr, R., Wood, J.D., Xu, X., Zuidema, P.A., 2021. Detecting forest response to droughts with global observations of vegetation water content. Glob. Change Biol. 27, 6005–6024. https://doi.org/10.1111/gcb.15872.

Lucas, R.M., Moghaddam, M., Cronin, N., 2004. Microwave scattering from mixed-species forests, Queensland, Australia. IEEE Trans. Geosci. Rem. Sens. 42, 2142–2159. https://doi.org/10.1109/TGRS.2004.834633.

McDonald, K.C., Zimmermann, R., Way, J., Chun, W., 1999. Automated instrumentation for continuous monitoring of the dielectric properties of woody vegetation: system design, implementation, and selected in situ measurements. IEEE Trans. Geosci. Rem. Sens. 37, 1880–1894. https://doi.org/10.1109/36.774701.

McDonald, K.C., Zimmermann, R., Kimball, J.S., 2002. Diurnal and spatial variation of xylem dielectric constant in Norway Spruce (Picea abies [L.] Karst.) as related to microclimate, xylem sap flow, and xylem chemistry. IEEE Trans. Geosci. Rem. Sens. 40, 2063–2082. https://doi.org/10.1109/TGRS.2002.803737.

Misra, G., Cawkwell, F., Wingler, A., 2020. Status of phenological research using sentinel-2 data: a review. Remote Sens. 12, 2760. https://doi.org/10.3390/rs12172760.

Moghaddam, M., Saatchi, S., 1995. Analysis of scattering mechanisms in SAR imagery over boreal forest: results from BOREAS '93. IEEE Trans. Geosci. Rem. Sens. 33, 1290–1296. https://doi.org/10.1109/36.469495.

Montzka, C., Bogena, H., Zreda, M., Monerris, A., Morrison, R., Muddu, S., Vereecken, H., 2017. Validation of spaceborne and modelled surface soil moisture products with cosmic-ray neutron probes. Remote Sens. 9, 103. https://doi.org/10.3390/rs9020103.

Munger, W., Hadley, J., 2023. Microclimate at harvard forest HEM, LPH and EMS towers since 2005. Harvard Forest Data Archive: HF206 27. https://doi.org/10.6073/PASTA/65DD1049CB0E25639457F535E39FADD8.

Notarnicola, C., Posa, F., 2007. Inferring vegetation water content from C- and L-band SAR images. IEEE Trans. Geosci. Rem. Sens. 45, 3165–3171. https://doi.org/10.1109/TGRS.2007.903698.

Orlowski, N., Rinderer, M., Dubbert, M., Ceperley, N., Hrachowitz, M., Gessler, A., Rothfuss, Y., Sprenger, M., Heidbüchel, I., Kübert, A., Beyer, M., Zuecco, G., McCarter, C., 2023. Challenges in studying water fluxes within the soil-plant-atmosphere continuum: a tracer-based perspective on pathways to progress. Sci. Total Environ. 881, 163510. https://doi.org/10.1016/j.scitotenv.2023.163510.

Owe, M., de Jeu, R., Holmes, T., 2008. Multisensor historical climatology of satellite-derived global land surface moisture. J. Geophys. Res. 113, F01002. https://doi.org/10.1029/2007JF000769.

Peel, M.C., Finlayson, B.L., McMahon, T.A., 2007. Updated world map of the Köppen-Geiger climate classification. Hydrol. Earth Syst. Sci. 11, 1633–1644. https://doi.org/10.5194/hess-11-1633-2007.

Quemada, C., Pérez-Escudero, J.M., Gonzalo, R., Ederra, I., Santesteban, L.G., Torres, N., Iriarte, J.C., 2021. Remote sensing for plant water content monitoring: a review. Remote Sens. 13, 2088. https://doi.org/10.3390/rs13112088.

Ruichen, M., Jinxi, S., Bin, T., Wenjin, X., Feihe, K., Haotian, S., Yuxin, L., 2023. Vegetation variation regulates soil moisture sensitivity to climate change on the Loess Plateau. J. Hydrol. 617, 128763. https://doi.org/10.1016/j.jhydrol.2022.128763.

Running, S., Mu, Q., Zhao, M., 2017. MOD16A2 MODIS/Terra net evapotranspiration 8-day L4 global 500m SIN grid V006. https://doi.org/10.5067/MODIS/MOD16A2.006.

Sato, A., Yamaguchi, Y., Singh, G., Park, Sang-Eun, 2012. Four-component scattering power decomposition with extended volume scattering model. Geosci. Rem. Sens. Lett. IEEE 9, 166–170. https://doi.org/10.1109/LGRS.2011.2162935.

Savitzky, Abraham, Golay, M.J.E., 1964. Smoothing and differentiation of data by simplified least squares procedures. Anal. Chem. 36, 1627–1639. https://doi.org/10.1021/ac60214a047.

Shen, X., Walker, J.P., Ye, N., Wu, X., Brakhasi, F., Boopathi, N., Zhu, L., Yeo, I.-Y., Kim, E., Kerr, Y., Jackson, T., 2022. Impact of random and periodic surface roughness on P- and L-band radiometry. Rem. Sens. Environ. 269, 112825. https://doi.org/10.1016/j.rse.2021.112825.

Ulaby, F.T., Long, D.G., 2014. Microwave Radar and Radiometric Remote Sensing. The University of Michigan Press, Ann Arbor.

Van Emmerik, T., Steele-Dunne, S.C., Judge, J., Van De Giesen, N., 2015. Impact of diurnal variation in vegetation water content on radar backscatter from maize during water stress. IEEE Trans. Geosci. Rem. Sens. 53, 3855–3869. https://doi.org/10.1109/TGRS.2014.2386142.

van Zyl, J.J., Arii, M., Kim, Y., 2011. Model-based decomposition of polarimetric SAR covariance matrices constrained for nonnegative eigenvalues. IEEE Trans. Geosci. Rem. Sens. 49, 3452–3459. https://doi.org/10.1109/TGRS.2011.2128325.

Weiss, T., 2015. Polarimetric Analysis of SAR Data to Estimate Plant Moisture in Agriculture, 2015. University of Munich, Germany. Master thesis, Faculty of Geoscience.

Wulder, M.A., Loveland, T.R., Roy, D.P., Crawford, C.J., Masek, J.G., Woodcock, C.E., Allen, R.G., Anderson, M.C., Belward, A.S., Cohen, W.B., Dwyer, J., Erb, A., Gao, F., Griffiths, P., Helder, D., Hermosilla, T., Hipple, J.D., Hostert, P., Hughes, M.J., Huntington, J., Johnson, D.M., Kennedy, R., Kilic, A., Li, Z., Lymburner, L., McCorkel, J., Pahlevan, N., Scambos, T.A., Schaaf, C., Schott, J.R., Sheng, Y., Storey, J., Vermote, E., Vogelmann, J., White, J.C., Wynne, R.H., Zhu, Z., 2019. Current status of Landsat program, science, and applications. Rem. Sens. Environ. 225, 127–147. https://doi.org/10.1016/j.rse.2019.02.015.

Yamaguchi, Y., Yajima, Y., Yamada, H., 2006. A four-component decomposition of POLSAR images based on the coherency matrix. Geosci. Rem. Sens. Lett. IEEE 3, 292–296. https://doi.org/10.1109/LGRS.2006.869986.